Precipitation and Mesoscale Convective Systems: Explicit versus Parameterized Convection over Northern Africa

Irene Reinares Martínez, Jean-Pierre Chaboureau

Precipitation and Mesoscale Convective Systems: Explicit versus Parameterized Convection over Northern Africa

IRENE REINARES MARTÍNEZ AND JEAN-PIERRE CHABOUREAU

Laboratoire d'Aérologie, Université de Toulouse, CNRS, UPS, Toulouse, France

(Manuscript received 13 July 2017, in final form 9 January 2018)

ABSTRACT

Precipitating systems are analyzed during a dust event from 9 to 14 June 2006 over northern Africa. A common analysis is applied to satellite observations and two Meso-NH simulations: one convection permitting (grid spacing $\Delta x = 2.5$ km) and the other with parameterized convection ($\Delta x = 20$ km). The precipitating systems are identified as cloud objects and classified as deep convective clouds (DCCs) or other clouds according to their infrared signature. Large DCCs [hereafter named mesoscale convective systems (MCSs)] are tracked, characterized in terms of precipitation and thermodynamic profiles, and analyzed in southern West Africa (SWA), central Africa, and Ethiopia. Precipitation is mostly observed along 0°–15°N, with 71% of the total precipitation produced by all DCCs and 55% by long-lived MCSs. It shows a marked diurnal cycle with a peak in the evening, mainly due to long-lived MCSs, which are characterized by an increase in size, zonal speed, and duration from east to west, with the largest, fastest, and longest-lived ones found over SWA. This is due to an enhanced African easterly jet (AEJ) and monsoon flow leading to stronger shear and greater conditional instability. The simulation with parameterized convection fails to distribute precipitation correctly. The convection-permitting simulation captures most of the observed precipitation features, but lacks the increase in organization of the long-lived MCSs over SWA. Excess moisture in a too zonal AEJ flow suggests that the long-lived MCSs in SWA are poorly located with respect to African easterly waves. The convection-permitting model improves the representation of precipitation but without fully resolving the long-lived MCSs.

1. Introduction

Precipitation over northern tropical Africa occurs mainly during the monsoon season. The summer rainfall can account for up to 95% of the total annual amount (e.g., in the Ethiopian Highlands; Segele and Lamb 2005). Most of the precipitation arises from moist convective instability (Bayo Omotosho 1985; Janiga and Thorncroft 2014), in the form of local thunderstorms or more organized systems such as mesoscale convective systems (MCSs). Precipitating systems start as individual convective cells triggered by the daytime boundary layer development, convergence lines, or other processes, preferentially in the lee of high terrain (Laing et al. 2008; Söhne et al. 2008). Their further growth into MCS is favored by midlevel dry air and the vertical wind shear associated with the African easterly jet (AEJ) (Laing et al. 2008; Janiga and Thorncroft 2014), a seasonal midlevel jet that results from the meridional temperature gradient between the Gulf of Guinea and the Sahara. Precipitation is significantly modulated by African easterly waves (AEWs) (Mathon et al. 2002; Fink and Reiner 2003; Laing et al. 2008), synoptic-scale disturbances of the AEJ having periods of 3–5 days and wavelengths of 2000–3000 km, with which the MCSs interact.

Precipitation over tropical Africa exhibits a marked diurnal cycle. In the first order, this is driven by solar heating. The morning increase of surface heat fluxes leads to the convective growth of the boundary layer, the moisture content of which is enriched by the monsoon flow. This leads to the generation of precipitating systems, usually in the afternoon, which is often followed by a westward propagation, primarily driven by the AEJ (Zhang et al. 2016). Over eastern Africa, convection is most commonly triggered in the afternoon along the western slopes of the Ethiopian Highlands (Laing et al. 2008). Over West Africa, most regions show a single diurnal peak of precipitation (Zhang et al. 2016). Afternoon peaks are generally associated with topographic features such as the Jos Plateau, and nocturnal peaks are due to precipitating systems downstream of high terrain

Corresponding author: Dr. Irene Reinares Martínez, irene.reinares@aero.obs-mip.fr

DOI: 10.1175/MWR-D-17-0202.1

(e.g., over Niamey and the northeastern part of Benin; e.g., Janiga and Thorncroft 2014; Zhang et al. 2016).

The contribution of MCSs to the total rainfall has been attributed to specific areas so far. Over southwest Niger, in the semiarid Niamey area (13°N, 2°E), their contribution has been estimated to be 90% (Mathon et al. 2002). Over Benin, in the semihumid Parakou area (9°N, 2°E), MCSs contribute to 50% (Fink et al. 2006). Over Nigeria, their contribution varies from 70% at 12°N down to 20% along the Guinean coast (Bayo Omotosho 1985). This southward decrease in contribution to precipitation has been explained by a decrease in the organization of MCSs (e.g., Bayo Omotosho 1985; Fink et al. 2006). The contribution of MCSs to rainfall over other regions, particularly over eastern tropical Africa, remains unknown, as does their contribution to the diurnal cycle of precipitation.

The aim of this paper is to examine the precipitating systems over northern Africa, particularly the characteristics and organization of MCSs. A combined analysis of MCSs and their dynamical and thermodynamical properties is attempted. It is impossible to guarantee the consistency between the cloud systems identified from satellite observations and the properties matched to them, taken from the European Centre for Medium-Range Weather Forecasts (ECMWF) operational analyses (which do not provide us with hydrometeor contents). Therefore, two simulations were run with the nonhydrostatic mesoscale atmospheric Meso-NH model (Lafore et al. 1998): one convection-permitting and the other with parameterized convection and different horizontal resolution. The difference in the simulation setup was not motivated by the desire to separate the effect of resolution and the effect of the representation of convection. The intention was rather to contrast two simulations: one typical of regional climate models and the other representative of convection-permitting models.

A rain-attribution methodology that associates rainfall with MCSs has been applied here to both satellite observations and simulations in the same way. In addition, profiles of thermodynamic quantities are determined for each MCS. The objectives are threefold: first, to give a comprehensive view of the sources of precipitation over northern tropical Africa; second, to show the performance of the Meso-NH model for each simulation, assessing, in particular, the ability of the simulations to reproduce the mechanisms controlling rain; and third, to analyze the properties of the MCSs and their degree of organization.

Rain has commonly been attributed to MCS by combining infrared imagery and rainfall information from rain gauges (e.g., Mathon et al. 2002; Fink et al. 2006) or from satellite observations, (e.g., Futyan and Del Genio 2007; Goyens et al. 2012). In the present study, deep convective clouds (DCCs) are identified by individual pixels with infrared brightness temperatures (BTs) lower than an arbitrary threshold. Contiguous DCCs are then clustered. Depending on their size, some DCC clusters are categorized as MCSs (and tracked in time) or as other convective systems. Rainfall information from satellite retrievals is matched with the DCC clusters, which enables the contribution of MCSs to precipitation to be estimated.

Our methodology is applied to the period from 9 to 14 June 2006, during a well-documented, intense dust outbreak (Flamant et al. 2009; Lemaître et al. 2010; Crumeyrolle et al. 2011). As shown in the following, the case of this relatively short, rainy period was selected because of the presence of propagating MCSs. Moreover, the presence of dust may modulate the AEJ through its direct radiative effect (e.g., Tompkins et al. 2005; Chaboureau et al. 2007). The radiative impact of dust on the MCS distribution over northern tropical Africa is, as yet, unstudied; however, it will be the subject of a companion paper. Here, our focus is on the characteristics of the precipitation distribution.

The article is structured as follows. The model and data, and the rain-attribution approach are described in sections 2 and 3, respectively. The overall distribution of clouds and precipitation and the diurnal cycle of precipitation are presented in section 4, where we show that MCSs contribute the most to precipitation. The propagation properties of MCSs and the environmental conditions in which they propagate are examined in section 5. The conclusions and some suggestions for further work are given in section 6.

2. Model and data

Two simulations are run using the anelastic, nonhydrostatic regional model Meso-NH (Lafore et al. 1998), version 5-1-3, over a domain of 3840×7680 km^2 (Fig. 1). Such a large domain over northern Africa allows both the AEWs propagation and the dust emissions in Chad and Sudan (Flamant et al. 2009) to be fully described. A regional run with a 20-km horizontal grid spacing (hereafter LowRes) is compared with a cloud-resolving run with a 2.5-km horizontal grid spacing (hereafter HiRes). Both runs use 72 vertical levels up to a height of 30 km, with vertical grid spacing between 60 and 600 m. HiRes uses about a third of a billion grid points, which is made possible by the large parallel computing capability of Meso-NH (Pantillon et al. 2011). The two simulations are run for the 6-day period from 0000 UTC 9 June to 0000 UTC 15 June 2006. The initial and boundary conditions are provided by the

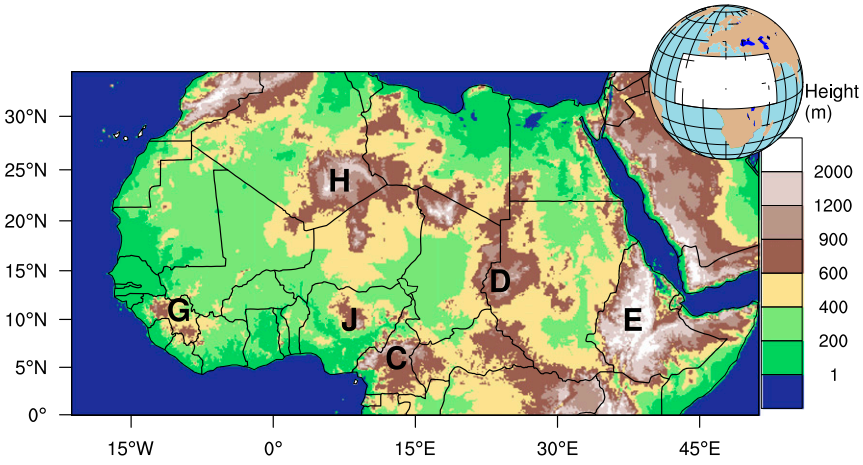

FIG. 1. Domain of simulation and analysis, with altitude color shaded. Topographic features are the Guinea Highlands (G), the Hoggar Mountains (H), the Jos Plateau (J), the Cameroon Highlands (C), the Darfur Plateau (D), and the Ethiopian Highlands (E).

ECMWF operational analysis. Model variables are output every 3 h.

Both runs use the Surface Externalisée (SURFEX) scheme for surface fluxes (Masson et al. 2013), a 1.5-order closure scheme for turbulence (Cuxart et al. 2000), and a parameterization of dry thermals and shallow cumuli (Pergaud et al. 2009). They further include a microphysical scheme for mixed-phase clouds (Pinty and Jabouille 1998), a subgrid statistical cloud scheme (Chaboureau and Bechtold 2005), and a dust prognostic scheme (Grini et al. 2006) to allow online interaction with radiation (the indirect effects of dust, i.e., the role of dust as cloud condensation nuclei or ice nuclei, are not considered here). The radiative scheme employed is the Rapid Radiative Transfer Model (Mlawer et al. 1997) for longwave radiation and the two-stream scheme (Fouquart and Bonnel 1986) for shortwave radiation. A subgrid deep convection scheme (Bechtold et al. 2001) is activated for LowRes while no deep convection parameterization is used for HiRes.

The capability of the Meso-NH simulations to capture the atmospheric dynamics is assessed by examining their kinetic energy spectrum following Skamarock (2004). Spectra of vertical velocities for HiRes and LowRes are computed at the end of the simulation (0000 UTC 15 June 2006), across the full domain and averaged between 3 and 9 km of altitude (Fig. 2). For the large scales, with wavelengths longer than 500 km corresponding to synoptic motions, both spectra show a wavenumber dependence of κ^{-3}, while they exhibit a $\kappa^{-5/3}$ dependence in the mesoscale. They both depart from the observational slope, but at different wavelengths: 200 km for LowRes against 20 km for HiRes. This is due to too large a removal of energy, which produces an energy removal grid-scale dependency. Each wavelength thus defines the effective resolution of each simulation (Skamarock 2004). This shows the added value offered by HiRes in resolving kinetic energy at convective scales.

Cloud systems are defined in terms of BT at 10.8 μm and 3-hourly accumulated precipitation is associated with them. From the model outputs, synthetic BTs corresponding to the Meteosat Second Generation (MSG)

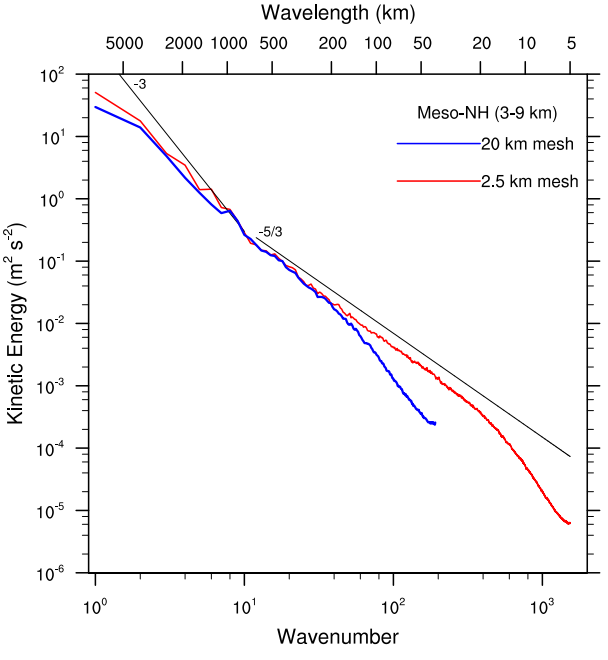

FIG. 2. Kinetic energy spectra of vertical velocities for HiRes ($\Delta x = 2.5$ km) and LowRes ($\Delta x = 20$ km) at 0000 UTC 15 Jun 2006, between 3 and 9 km of altitude. The theoretical power laws at -3 and $-5/3$ are shown with black lines.

observations are computed offline using the Radiative Transfer for the Television and Infrared Observation Satellite (TIROS) Operational Vertical Sounder (RTTOV) code, version 8.7 (Saunders et al. 2005), as previously used by Chaboureau et al. (2008). Two observation datasets are used to assess the simulations: the globally merged 4-km-resolution BT data (Janowiak et al. 2001), merged from all available geostationary satellites and provided by the Climate Prediction Center, and the 3-hourly product 3B42, version 7 (Huffman et al. 2007), from the Tropical Rainfall Measuring Mission (TRMM) available in 0.25° spatial resolution. The gridded BT data eases the comparison with the model outputs while the temporal sampling of the TRMM 3B42 product is convenient for the analysis of the diurnal cycle of precipitation, a feature that results in the TRMM 3B42 product being widely employed (e.g., Janiga and Thorncroft 2014; Zhang et al. 2016).

3. Rain-attribution approach

Clouds and their associated precipitation are analyzed in a grid mesh of 20 km for all the datasets. Such a common grid mesh is necessary to analyze the observation datasets, which have a different resolution (4 km for MSG against 0.25° for TRMM). The sensitivity of the cloud size distribution to the resolution further requires the same grid mesh to be used. We then define two cloud categories. Following many others (e.g., Mathon et al. 2002; Tian et al. 2004; Laing et al. 2008; Söhne et al. 2008), DCCs are diagnosed for BT less than 230 K while cirrus anvil clouds (CACs) are identified for BTs ranging between 230 and 260 K. Because the simulated BTs are biased toward higher values (mostly because of model errors in the location and height of cloud cover; Fig. 3a), we use different BT thresholds for the simulations. They are defined in such a way that each cloud category is equally represented over the 6-day period whatever the dataset. In other words, the thresholds are adjusted so that the number of DCCs and CACs is the same in both the observations and the simulations. This leads to the thresholds of 243 and 266 K for HiRes and 246 and 264 K for LowRes. From Fig. 3a, it can be noted that the simulated BTs corresponding to the DCC category are generally higher than observed. This is more pronounced for LowRes. It suggests that DCCs may be shallower for LowRes with respect to HiRes, and may present a lower content of iced hydrometeors. This could eventually lead to a reduction of precipitation.

The 3-hourly accumulated precipitation is attributed to each 20-km grid point. Note that daily amounts of precipitation of less than 0.2 mm are considered as traces (WMO 2014) and are excluded from the analysis. Figure 3b shows that they are very frequent (52% for TRMM, 56% for HiRes, and 36% for LowRes). Ruling out these grid points with trace values nevertheless allows us to consider 99.5% of the total precipitation whatever the dataset. The frequency of grid points in the range between 0.2 and 10 mm day^{-1} is approximately 40% for TRMM and HiRes, and 57% for LowRes. The production of many cells with low intensity rainfall is a well-known failure of parameterized convection. Grid points with precipitation in this range produce 48% of total precipitation for TRMM and about 10% more for the simulations. Precipitation rates between 10 and 50 mm day^{-1} represent 5%, 7%, and 8% for HiRes, LowRes, and TRMM, respectively. In TRMM, this represents 51% of total precipitation, approximately 12% greater than in the simulations. Precipitation rates over 50 mm day^{-1} are more frequent for HiRes (0.08%) than for TRMM (0.03%) or LowRes (0.05%) and they produce more precipitation for HiRes (2%) than for TRMM (0.5%) or LowRes (1%). Still, the precipitation rates shown in Fig. 3b present a lower cutoff for HiRes as a consequence of precipitation being regridded to a 20-km resolution. Regridding precipitation acts to smooth the extreme values, which also explains the less frequent precipitation rates over 50 mm day^{-1} found for TRMM compared to LowRes.

DCC and CAC grid points are then aggregated into clusters. We define clusters as contiguous grid points of the same cloud category. Grid points are considered contiguous only if they share a common face. Each DCC cluster is further associated with 3-hourly accumulated precipitation and vertical profiles of thermodynamic variables. For the observed clusters, the precipitation is obtained from TRMM while the vertical profiles are taken from the ECMWF analysis at 0000, 0600, 1200, and 1800 UTC and from the ECMWF 3-h forecasts at 0300, 0900, 1500, and 2100 UTC. For the simulated clusters, the precipitation and profiles are taken from the model outputs. The profiles associated with each DCC cluster are computed in the volume generated when the envelope of the cluster is projected into the vertical. They are calculated both at the time of the detection and 6 h before at the same location. This allows us to analyze the properties of the DCC clusters and of their environmental conditions prior to their detection, respectively. An example of the rain-attribution method applied to the observation is shown at 2100 UTC 11 June (Fig. 4). This time is selected because DCCs of different sizes are located all over northern tropical Africa (Fig. 4a). The 3-hourly accumulated precipitation is attributed to all of them (Fig. 4b).

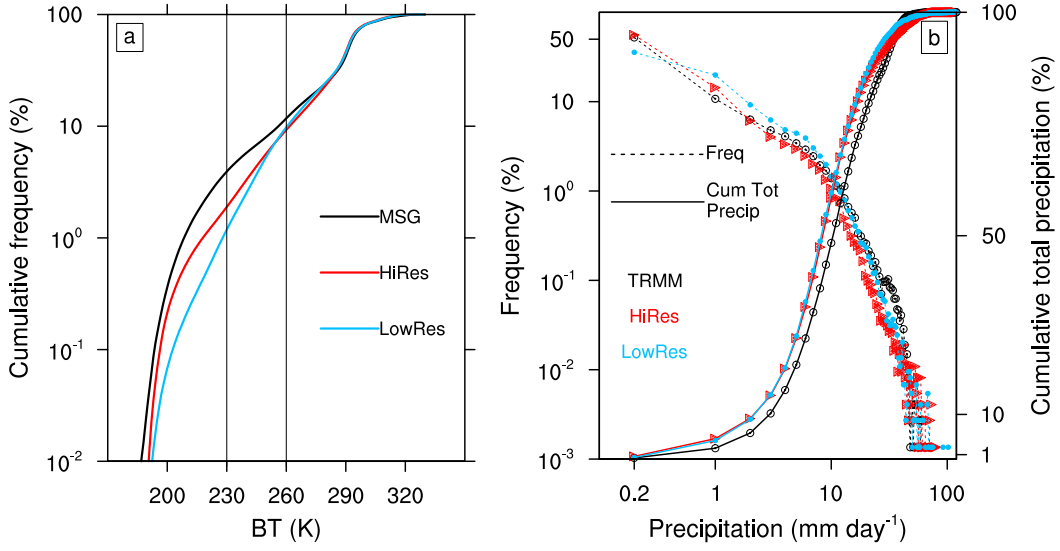

FIG. 3. (a) Cumulative distribution function of brightness temperature at 3-h resolution on a 20-km grid for MSG, HiRes, and LowRes. (b) Distribution function of total accumulated precipitation over the 6-day period by class of 1 mm day^{-1} on a 20-km grid for TRMM, HiRes, and LowRes.

Finally, a tracking method is used to follow DCCs and their characteristics over time. Geographical overlapping between successive BT images has been extensively used (e.g., Machado et al. 1998; Mathon et al. 2002; Fink et al. 2006), with different surface overlapping ratios. After testing several overlapping ratios in the range between 5% and 35%, we set the ratio to 20%. This produces the most realistic trajectories (i.e., trajectories that match results found in the literature in terms of number, propagation speed, and duration of the tracked cloud systems) (e.g., Machado et al. 1998; Goyens et al. 2012). Machado et al. (1998) suggest considering only clusters larger than 10 000 km^2 when the temporal resolution of the satellite images is greater than 3 h. Because the tracking is done on a 3-hourly basis, it is applied only to clusters with an effective diameter larger than 120 km, equivalent to an area of 11 300 km^2. The effective diameter is defined as the diameter of a circle having an area equal to that of the DCC. In the following, DCCs that satisfy this threshold on the effective diameter are called MCSs, and the rest small DCCs. Then, MCSs are divided into two categories according to their lifetime. Long-lived MCSs last at least 6 h and short-lived MCSs last less than 6 h. Three subregions (Fig. 4a) are considered to cover most of the continental tropical band within the domain while contrasting in the atmospheric conditions in which MCSs developed, as will be shown later: southern West Africa (SWA), central Africa (CAF), and Ethiopia (ETH).

4. Overview of clouds and precipitation

a. Distribution

The spatial distribution of DCCs and precipitation is shown in Fig. 5. DCCs are observed south of 15°N in a zonal band that extends from the Atlantic Ocean to 40°E, the monsoon trough. DCCs are also visible over Algeria, near the foothills of the Hoggar Mountains (Fig. 5a). They are the most frequent over the eastern Atlantic and the Ethiopian Highlands. Precipitation is also observed over the zonal band but not over Algeria (Fig. 5d). Accumulated rainfall values are highest over the eastern Atlantic and the Ethiopian Highlands, consistent with the locations found for the highest frequencies of DCCs. Over the continent, precipitation is mainly found south of the intertropical discontinuity (ITD) defined as the continental boundary that separates the northeasterly dry, warm harmattan flow and the southwesterly cold, moist monsoon flow. Most of the continental precipitation occurs inside the three subregions previously defined (Fig. 5d). In SWA, the precipitation presents the greatest values west of the Jos Plateau, over the center of Benin and over the flatter regions around the border of Ivory Coast, Ghana, and Burkina Faso. In CAF, the precipitation is maximum around the northern border of Democratic Republic of Congo, the southwestern region of central Africa and in southern Chad. In ETH, precipitation is mostly distributed over the Ethiopian Highlands, where the maximum values appear on the western slopes.

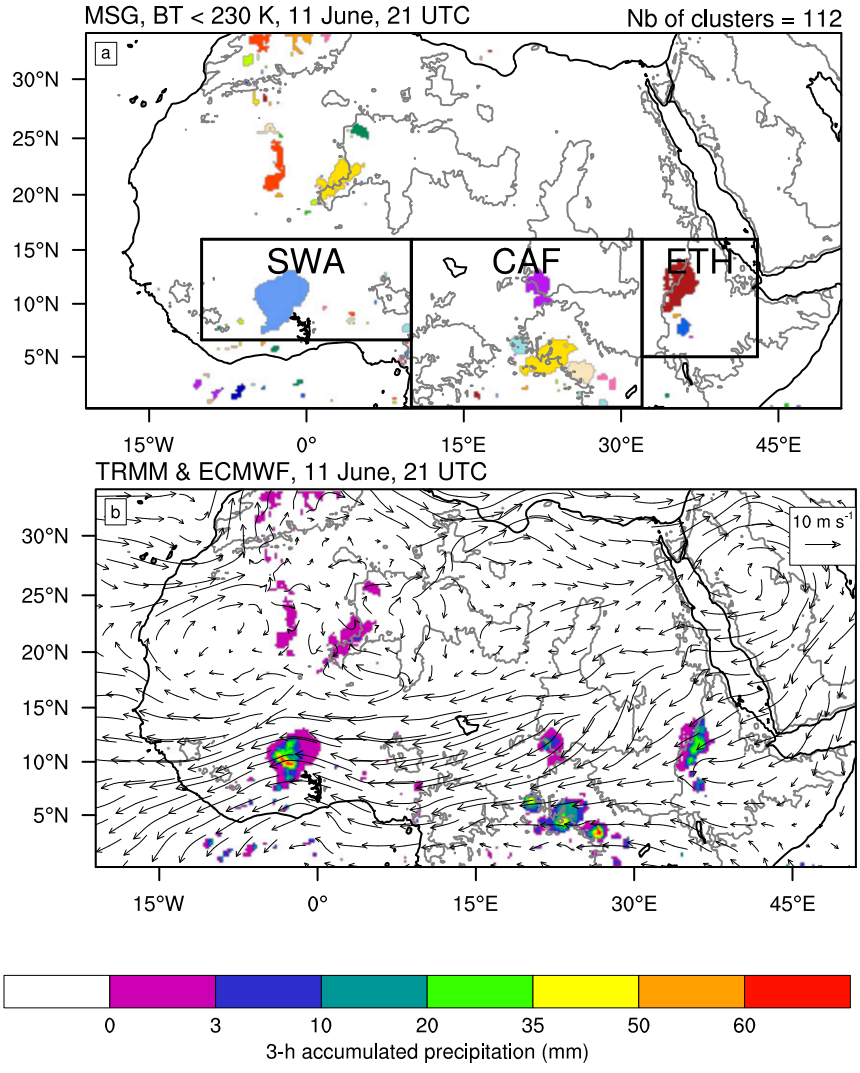

FIG. 4. (a) Example of the identification of DCC clusters at 2100 UTC 11 Jun 2006. A color is assigned to each cluster. (b) The attribution of 3-h accumulated precipitation from TRMM product 3B42 to each cluster in (a). The solid gray lines represent the orography at 600-m altitude. In (a), the black squares delimit three subregions: southern West Africa (SWA), central Africa (CAF), and Ethiopia (ETH).

In both simulations, the zonal patterns of DCCs and precipitation are reproduced well. DCCs are, however, missing over the Gulf of Guinea close to the southern limit of the simulation domain. The development of clouds is inhibited there by the strong southwesterly monsoon inflow. DCCs are overestimated over the Gulf of Guinea along almost all of the coast. DCCs and precipitation show a reduced extension over the eastern Atlantic, with DCCs being too frequent and precipitation too weak. This is more marked in HiRes than in LowRes. Moreover, in the HiRes simulation, precipitation exceeds 40 mm day^{-1} over the coast of Sierra Leone and Liberia, whereas, for TRMM, we find lower values, of up to 30 mm day^{-1}. Finally, simulated DCCs are more frequent over the Ethiopian Highlands and much more widespread over Algeria than observed. Furthermore, LowRes produces more precipitation over Algeria than TRMM and HiRes.

The total precipitation caused by different cloud categories is computed by associating 3-hourly accumulated precipitation with the clusters of different cloud categories (Fig. 6). In the observations, 71% of total precipitation comes from DCCs and 19% is due to CACs. The remaining precipitation (10%) is attributed to clouds other than DCCs or CACs. Long-lived MCSs account for 55% of precipitation, short-lived MCSs for

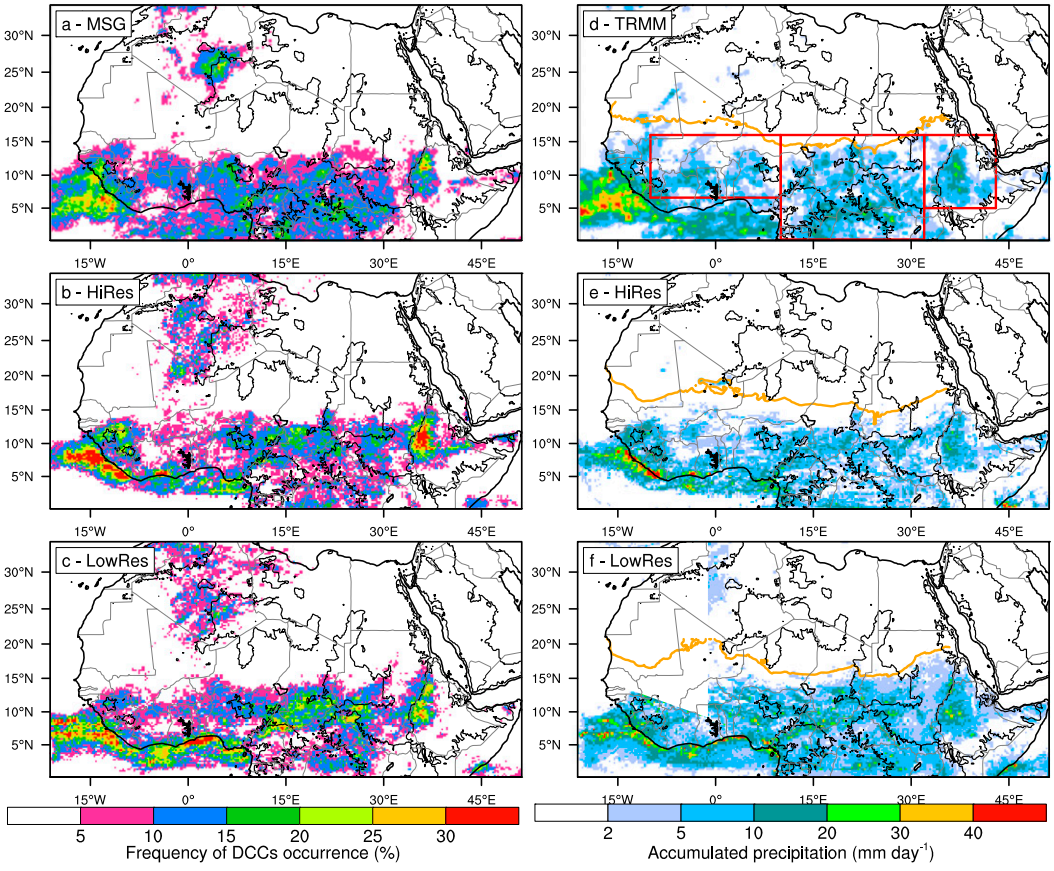

FIG. 5. (left) Frequency of occurrence of DCCs during 9–14 Jun 2006 for (a) MSG, (b) HiRes, and (c) LowRes. (right) Mean total accumulated precipitation during the same period for (d) TRMM, (e) HiRes, and (f) LowRes. The solid black lines show the orography at 600-m altitude. In (d), the red squares delimit the subregions as in Fig. 4a. The orange lines in (d)–(f) show the ITD defined as where the average water vapor mixing ratio at 2 m equals 10 g kg^{-1} (Chaboureau et al. 2016).

11% and the remaining 5% comes from small DCCs. Therefore, MCSs produce 66% of total precipitation, which is in the range of contributions found for different regions in West Africa (e.g., Mathon et al. 2002; Fink et al. 2006; Bayo Omotosho 1985). HiRes reproduces this distribution well, with 66% of precipitation coming from DCCs, 17% from CACs, and 17% from other clouds. Long-lived MCSs produce 50% of precipitation, short-lived MCSs contribute to 10%, and small DCCs to 6%. Thus, long-lived MCSs in HiRes are the first contributors to precipitation as observed. LowRes is not able to reproduce this feature as long-lived MCSs produce only 29% of precipitation, a contribution similar to that of CACs (24%) and other clouds (33%). In fact, clouds other than DCCs are the main contributors to precipitation. In LowRes, for which deep convection is parameterized, 70% of the total precipitation is produced by the parameterization while the DCCs only produce 43% of precipitation. One reason is that the parameterization inhibits the vertical development of the DCCs, which present too low a hydrometeor content. This was previously pointed out from Fig. 3a.

The observed MCSs cover a surface of almost 11 million km^2 over the 6 days and they produce 66% of total precipitation (Fig. 6). In the simulations, the MCSs cover about the same surface area (98% of what is observed) but contribute less to total precipitation. In fact, HiRes produces 6% less precipitation. This means that precipitation caused by MCSs in HiRes is less intense than observed, with less precipitation produced per unit area. In LowRes this is more pronounced, with 30% less precipitation.

b. Diurnal cycle of precipitation

The diurnal cycle of precipitation is examined in Fig. 7. Over land, the observed diurnal cycle has an amplitude of 0.37 mm day^{-1} and a maximum value of 0.56 mm day^{-1} at 2100 LST (Fig. 7a). For HiRes the

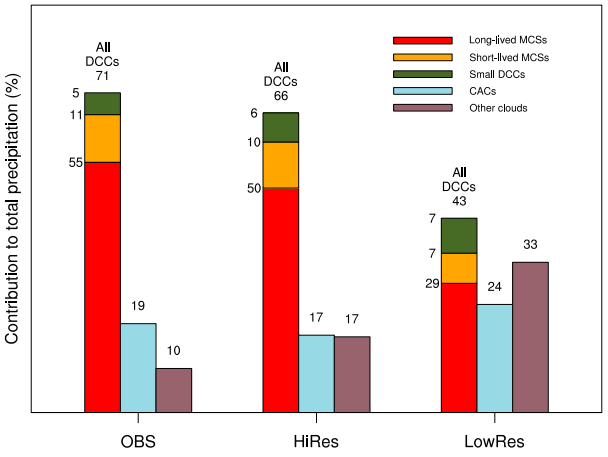

FIG. 6. Contribution of all the DCCs (long- and short-lived MCSs and small DCCs), CACs, and other clouds to total precipitation over the whole domain for the observations and the simulations.

observed amplitude, the maximum rainfall rate, and the time of peak precipitation are well reproduced (0.34 mm day^{-1}, 0.55 mm day^{-1}, and 2100 LST, respectively). However, HiRes lacks precipitation between 0000 and 0900 LST, up to 0.2 mm day^{-1}. LowRes also shows a diurnal cycle with similar amplitude and maximum values (0.38 and 0.60 mm day^{-1}) but it peaks earlier, at 1500 LST, a common feature of parameterized convection in the tropics. Over the ocean (Fig. 7b), the diurnal cycle is less pronounced than over land, with amplitudes of 0.12, 0.10, and 0.08 mm day^{-1} for the observations, HiRes, and LowRes, respectively. This result can be explained by the fact that the ocean has a greater thermal inertia than the land. The maxima over the ocean occur at 0900 LST and the simulations lack precipitation (as shown previously in the southern limit of the simulation domain).

Because continental precipitation explains the diurnal cycle of total precipitation at first order, the diurnal cycle over land is further analyzed by partitioning it according to the different cloud categories (Figs. 7c,d). For the observations, long-lived MCSs show the largest values for precipitation, larger than 0.1 mm day^{-1}. This is expected as the observed long-lived MCSs contribute the most to the total precipitation (55%). They present the highest values of precipitation between 1800 and 0300 LST, over the same time range as for the precipitation over land. Thus, long-lived MCSs over land explain most of the diurnal cycle of precipitation. Clouds other than DCCs are the second greatest contributors to the diurnal cycle, with values between 0.06 and 0.2 mm day^{-1}. This is also expected as these clouds are the second contributors to the total precipitation (29%). Their peak at 1800 LST suggests that these clouds are sensitive to the diurnal cycle of surface fluxes over land. Short-lived MCSs are the third contributors to the total precipitation, with a diurnal variation of approximately 0.05 mm day^{-1}. Precipitation resulting from short-lived MCSs shows two peaks, around 0600 and 2100 LST. Last, small DCCs present fairly constant precipitation with respect to time, of around 0.02 mm day^{-1}.

HiRes reproduces the distribution of total precipitation among cloud categories well, as seen in Fig. 6, but it underestimates the contribution of long-lived MCSs between 0000 and 1200 LST by almost 0.2 mm day^{-1}. It also overestimates the contribution of clouds other than DCCs by about the same amount at 1200 and at 0000 LST. HiRes lacks precipitation for short-lived MCSs between 0300 and 0600 LST, of about 0.05 mm day^{-1}, because precipitation from short-lived MCSs is single peaked for HiRes. In summary, the success of HiRes in capturing the total precipitation over land between 1200 and 2100 LST comes partly from compensating errors between the different contributors. The lack of nocturnal precipitation over land after midnight in HiRes is due to long-lived and short-lived MCSs, and clouds other than DCCs.

For LowRes, the main contribution to the diurnal cycle of precipitation comes from clouds other than DCCs, with values ranging between 0.1 and 0.4 mm day^{-1}. This is expected as these clouds contribute to 57% of the total precipitation. The peak in precipitation at 1500 LST resulting from these clouds mainly explains the early peak in total precipitation over land. This peak is mainly controlled by the precipitation produced by the convective parameterization, which is also maximum at 1500 LST (not shown). The second contributor is long-lived MCSs, with values in their diurnal cycle of between approximately 0.1 and 0.2 mm day^{-1}. LowRes underestimates the contribution of long-lived MCSs by at least a factor of 2. It is, however, able to reproduce the phase of the diurnal cycle correctly. Another drawback concerns the double peaks in precipitation missed for the short-lived MCSs, as pointed out for HiRes, and the overestimation of afternoon precipitation for small DCCs.

The differences in the diurnal cycle of precipitation resulting from long-lived MCSs are further analyzed by subregion (Fig. 8). For HiRes (Figs. 8a–d), continental long-lived MCSs lack precipitation after midnight, while producing an excess of precipitation in the afternoon. This can be explained by a compensating effect between an excess of precipitation over ETH between 1500 and 2100 LST and a systematic deficit in precipitation over SWA and CAF. For LowRes (Figs. 8e–h), the deficit in precipitation caused by long-lived MCSs also comes mostly from SWA and CAF. Precipitation is best captured over ETH in both simulations, which can be explained by the strong orographic enhancement of precipitation there.

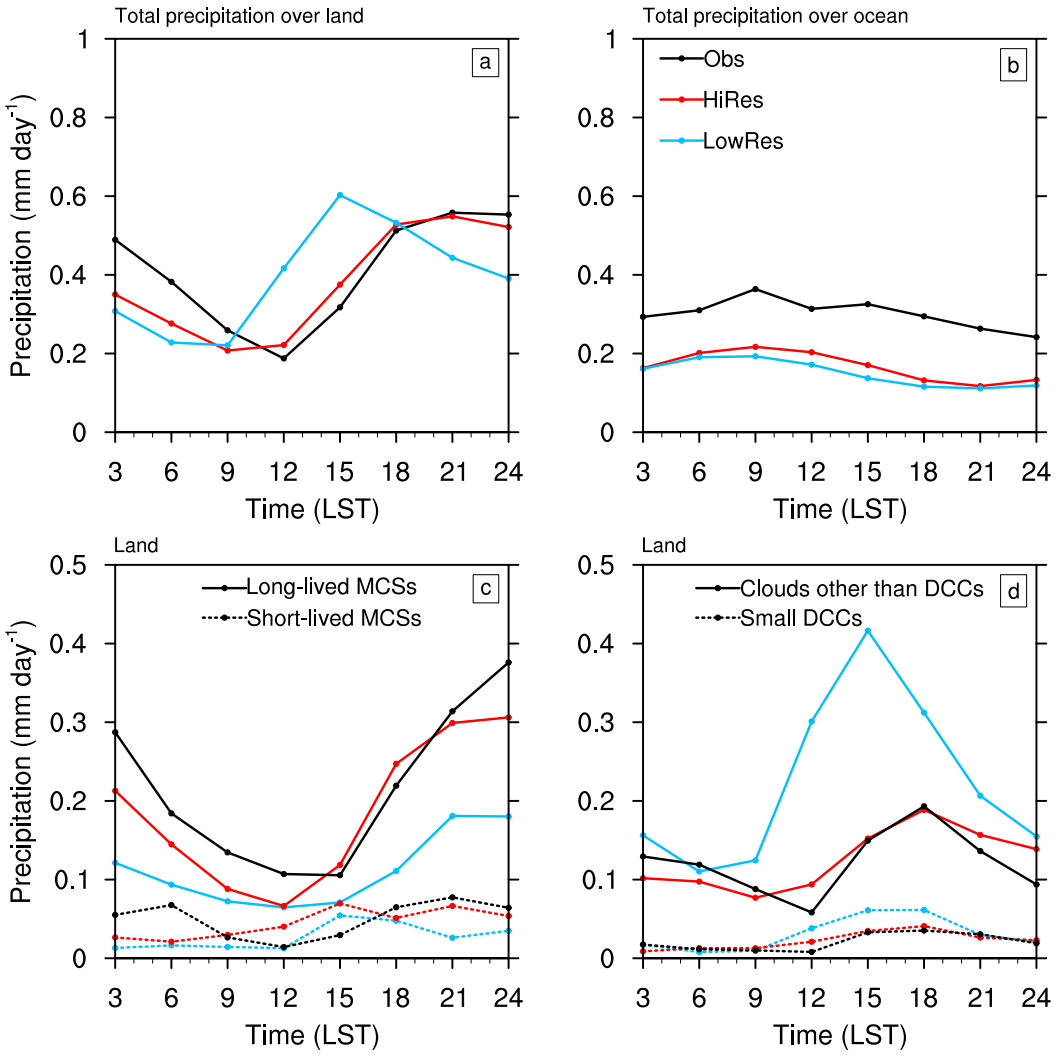

FIG. 7. Diurnal cycle of (a) precipitation over land, (b) precipitation over ocean, (c) precipitation over land due to long-lived MCSs and short-lived MCSs, and (d) precipitation over land due to clouds other than DCCs (e.g., CACs and other clouds), and small DCCs for the observations and both simulations.

5. Characteristics of long-lived MCSs by subregion

a. Size and propagation

Because long-lived MCSs account for most of the observed precipitation, it is essential to describe such systems and to evaluate the capability of the simulations to statistically reproduce the characteristics of their population. The trajectories of long-lived MCSs are depicted in Fig. 9. Their number decreases with the duration whatever the dataset, as found by others (e.g., Fink et al. 2006; Laing et al. 2008). In the regions where long-lived MCSs form and grow, favorable conditions provide them with energy that will eventually decay unless the long-lived MCSs are enhanced during their propagation. Laing et al. (2008) argue that an approximately exponential decay of the number of MCSs over their lifetime is expected. Among the 62 observed trajectories, which have an average lifetime of 11.3 h, the majority start over the continent. The observed long-lived MCSs are first detected over the Ethiopian Highlands, near the borders of the Darfur Plateau and the Cameroon Highlands in CAF, the borders of the Jos Plateau in SWA, and to the west of SWA, close to the Guinea Highlands. Over the ocean, long-lived MCSs are first detected mostly on the Gulf of Guinea. The long-lived MCSs propagate principally from east to west, within the AEJ. For the simulations, they are more numerous and shorter lived than observed (84 with an average duration of 10.7 h for HiRes and 104 with a duration of 10.4 h for LowRes). Their first detections are spatially distributed in a similar way to observations for both simulations.

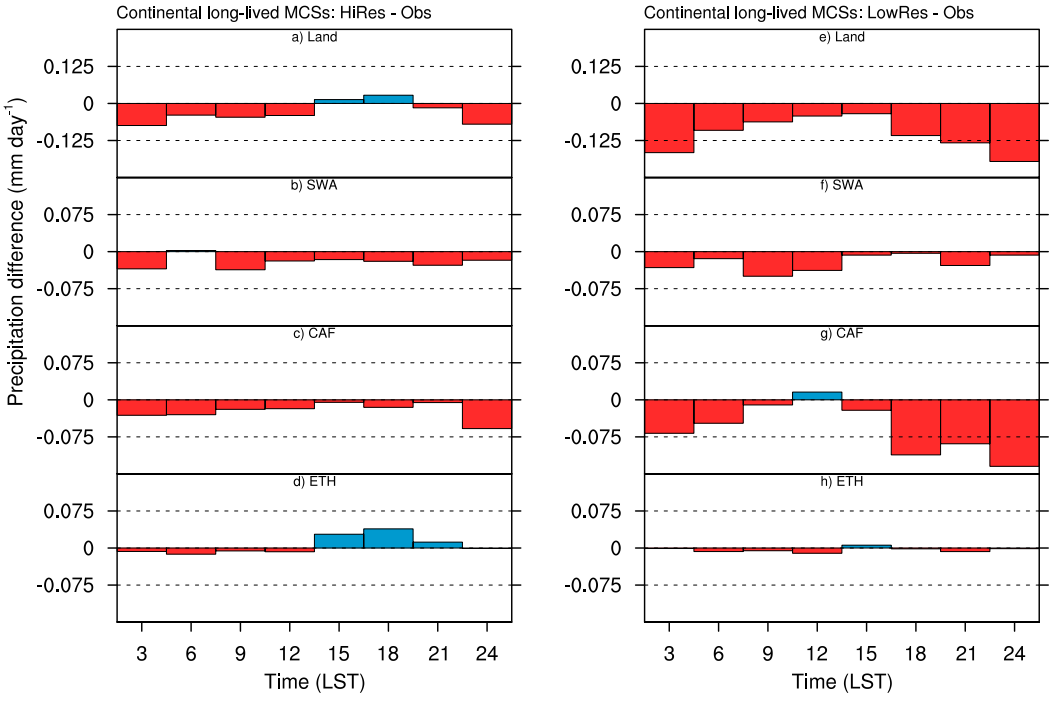

FIG. 8. Differences in the diurnal cycle of precipitation due to long-lived MCSs between (left) HiRes and the observations and (right) between LowRes and the observations for (a),(e) land; (b),(f) SWA; (c),(g) CAF; and (d),(h) ETH.

The propagation characteristics of long-lived MCSs by subregion are shown in Fig. 10. A trajectory is associated with the subregion where the long-lived MCS spends most of its lifetime (i.e., where the majority of the MCS track points shown in Fig. 10 lie). Zonal and meridional speeds are computed for each MCS, using their locations between their first and last detections. Observed long-lived MCSs are first detected mostly over CAF. Their effective diameter increases from east to west, from 300 km over ETH to 600 km over SWA. Their duration is about 10 h over ETH and CAF and 20 h over SWA. They have an average zonal speed of $-8.5\,\mathrm{m\,s^{-1}}$ in ETH, $-10.1\,\mathrm{m\,s^{-1}}$ in CAF, and $-17.8\,\mathrm{m\,s^{-1}}$ in SWA. Their meridional speeds are lower in absolute value; they are 2.1, 2.5, and $-1.5\,\mathrm{m\,s^{-1}}$ for ETH, CAF, and SWA, respectively. Thus, while the observed long-lived MCSs mainly propagate westward, they present a northward component in ETH and CAF, and a southward component in SWA. The long-lived MCSs over SWA are the most organized. They are the largest, fastest, and longest-lived MCSs of all the subregions.

Both simulations overestimate the number of long-lived MCSs over the three subregions, the number is 44% greater for HiRes and 93% greater for LowRes. The 44% excess for HiRes is close to the 53% overestimate of MCS tracks found in a 6-day convection-permitting simulation over West Africa (Beucher et al. 2014). For HiRes, many of the too numerous long-lived MCSs over ETH are simulated in the afternoon (not shown), which may explain the excess of afternoon precipitation (Fig. 8d). The increase in effective diameter of long-lived MCSs from east to west is not reproduced by the simulations. The effective diameter remains the same in the three subregions. It is, therefore, well captured over ETH but too low over CAF and strongly underestimated over SWA. The duration of long-lived MCSs is correctly simulated in CAF and ETH, but too low over SWA. In both simulations, the long-lived MCSs propagate westward, and are the fastest over SWA. For HiRes, the zonal speed over SWA is, however, about one-third lower than observed (-11.5 vs $-17.8\,\mathrm{m\,s^{-1}}$). For LowRes, the long-lived MCSs are too slow in all the three subregions. LowRes simulates the observed northward propagation of long-lived MCSs in CAF and ETH and the southward propagation in SWA, but long-lived MCSs for HiRes are too westward directed.

In summary, the long-lived MCSs are observed to increase their size, lifetime, and propagation speed from ETH to SWA. In a general way, the main propagation characteristics of long-lived MCSs, such as their number, diameter, lifetime, and propagation speed are better

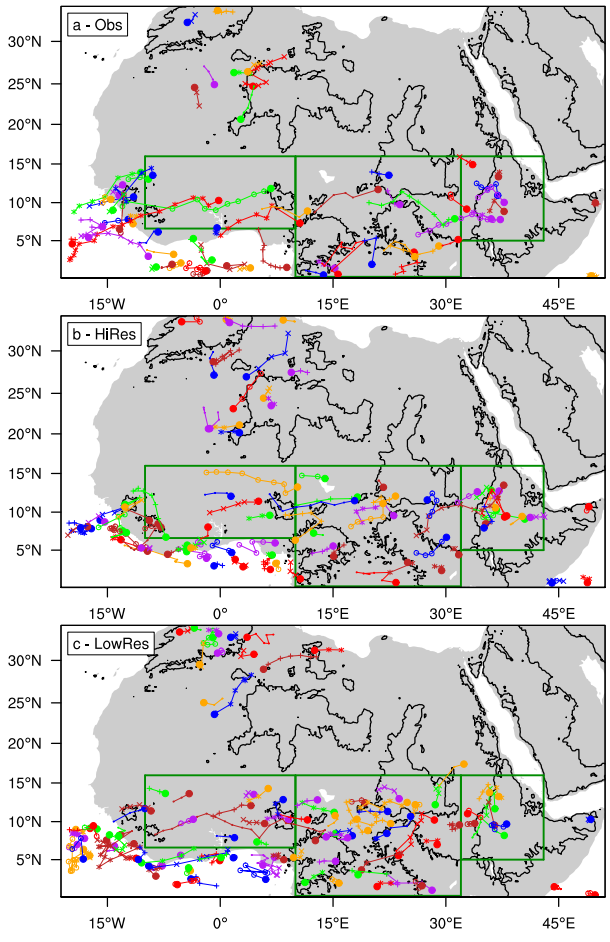

FIG. 9. Tracked trajectories of long-lived MCSs (duration of at least 6 h) for (a) the observations, (b) HiRes, and (c) LowRes. The dots represent the first detection of each MCS. The changing colors among trajectories have no significance. The solid black lines show the orography at 600-m altitude.

captured by HiRes than by LowRes. Nevertheless, HiRes presents strong biases over SWA, notably as the long-lived MCSs show a weak degree of organization and an incorrect meridional propagation.

b. *Environmental conditions*

To understand why the long-lived MCSs differ with the subregion, we examine the environmental conditions in which these MCSs develop (Fig. 11). In the observations, near-surface moisture is maximum over SWA, with a value of water vapor mixing ratio of $16\,g\,kg^{-1}$, and the low- to midlevel atmosphere presents the strongest vertical gradient of equivalent potential temperature θ_e. In other words, the conditional instability is the greatest there. This can lead to convection being more intense over SWA when triggered. The speed of the AEJ, located at around 4-km altitude with an easterly direction, increases from east to west. Its maximum ranges from $8\,m\,s^{-1}$ over ETH, to $10\,m\,s^{-1}$ over CAF, and to $16\,m\,s^{-1}$ over SWA, where the AEJ is the strongest, in agreement with the zonal propagation speed of long-lived MCSs (Fig. 10). Between 0.8- and 2-km altitude, the wind direction changes abruptly. Below 2 km the average southwesterly flow corresponds to the monsoon flow. Note that the variability in the wind direction among the individual profiles is much greater in the lower atmosphere than aloft. This is mostly due to the diurnal variability associated with solar heating, which affects the boundary layer circulation. In mountainous areas like ETH, the orography can also play a partial role, as the slope breeze modulates the monsoon flow. Thus, a strong vertical shear is found between the low-level southerly and the midlevel easterly flows, with the largest values over SWA.

HiRes reproduces the observed profiles of water vapor mixing ratio over CAF and SWA very well, but overestimates the water vapor mixing ratio above 2-km altitude over SWA. For example, at 2.8-km altitude, HiRes shows a value of $7.7\,g\,kg^{-1}$ compared to $6.5\,g\,kg^{-1}$ for the observations. LowRes shows a persistent increase in water vapor mixing ratio at the low level and a deficit at the midlevel, in all the three subregions. This is consistent with insufficient injection of moisture through convective updrafts. The increase in both the convective instability and AEJ speed from ETH to SWA is captured by the simulations. The mean monsoon flow is generally overestimated for LowRes, and also for HiRes over SWA. The poor reproduction of the propagation of the long-lived MCSs by HiRes over SWA may be due to differences between the observations and HiRes in the wind at altitudes around 3 km, the steering level for MCS propagation. Indeed, its mean direction is 77° for the observations and 84° for HiRes. Moreover, the meridional wind at 3-km altitude for HiRes shows the greatest variability in intensity over SWA. For some individual profiles, it is southerly, indicating that moist air is advected northward to SWA (not shown).

c. *Properties of long-lived MCSs*

To examine the convective response to the larger-scale environmental forcing, average profiles of the long-lived MCSs are shown in Fig. 12. Each MCS is associated with the subregion where it spends most of its lifetime. For both simulations, liquid hydrometeors appear mostly up to the freezing level, around 4 km, with a drastic reduction above. A small amount of supercooled water is present up to 9 km, before the cloud droplets freeze completely. The solid hydrometeor content increases above 4 km, reaching a maximum around 9 km, and is nonzero up to 17 km, approximately the height of the tropopause. The release of latent heat through the

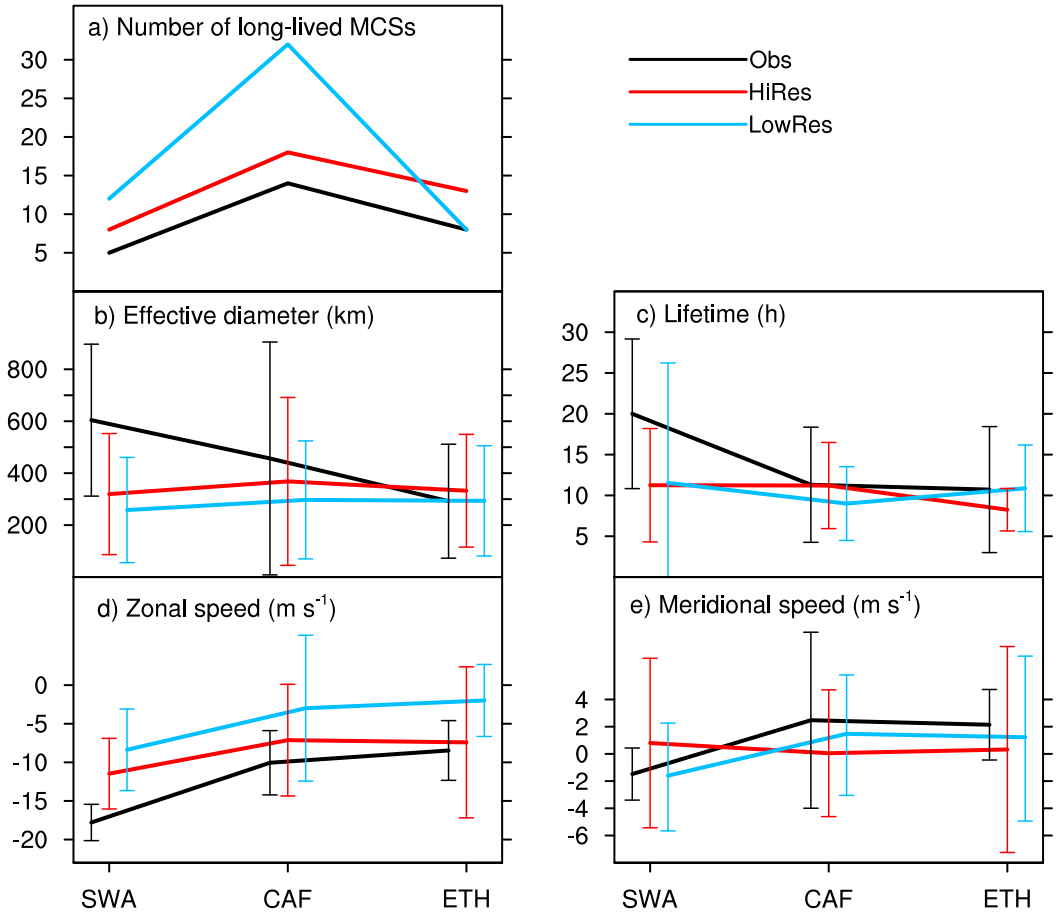

FIG. 10. Characteristics of long-lived MCSs by subregion (SWA, CAF, and ETH) for the observations and the simulations: (a) number of first detections, (b) effective diameter, (c) duration, (d) zonal speed, and (e) meridional speed. In (b)–(e), the solid lines represent the mean values and the error bars represent the standard deviation.

freezing of liquid particles and the deposition of water vapor accelerates the air parcels, which show the greatest upward velocities between altitudes of 6–9 km. Over SWA and CAF, both the hydrometeor loading and upward velocities are larger than over ETH, as there is more convective instability. Over SWA and CAF the freezing level and maximum upward speeds are reported to be 1 km higher than over ETH. The updrafts and downdrafts are stronger for HiRes than for LowRes, an effect of the fully explicit representation of convection and the horizontal resolution. The cold, dry subsiding air is diagnosed by a decrease in θ_e in the lower 3 km between the conditions before and at the time of convection, which has the effect of stabilizing the atmosphere. The reduction of θ_e, which is a signature of cold pools, increases from ETH to SWA. This drop is greater for HiRes than LowRes whatever the subregion. The most intense cold pools are found over SWA for HiRes, where, in the lowest 500 m, there is an average decrease of θ_e of up to 10 K. However, the presence of a layer of insufficiently dry air at 3-km altitude, which feeds the cold pools, could result in the pools not being intense enough. The too slow propagation of the long-lived MCSs over SWA in HiRes and their reduced duration could be a consequence of simulating cold pools that are too weak.

6. Conclusions

This study examines continental precipitating systems over northern Africa from 9 to 14 June 2006. A common method is applied to the observations and to two simulations (convection permitting and with parameterized convection), for which MCSs are tracked and their properties analyzed in detail over southern West Africa (SWA), central Africa (CAF), and Ethiopia (ETH).

The analysis of the observations shows that continental precipitation is distributed over a zonal band south of the ITD, from the Ethiopian Highlands to the Atlantic. The highest precipitation rates and the maximum of DCCs

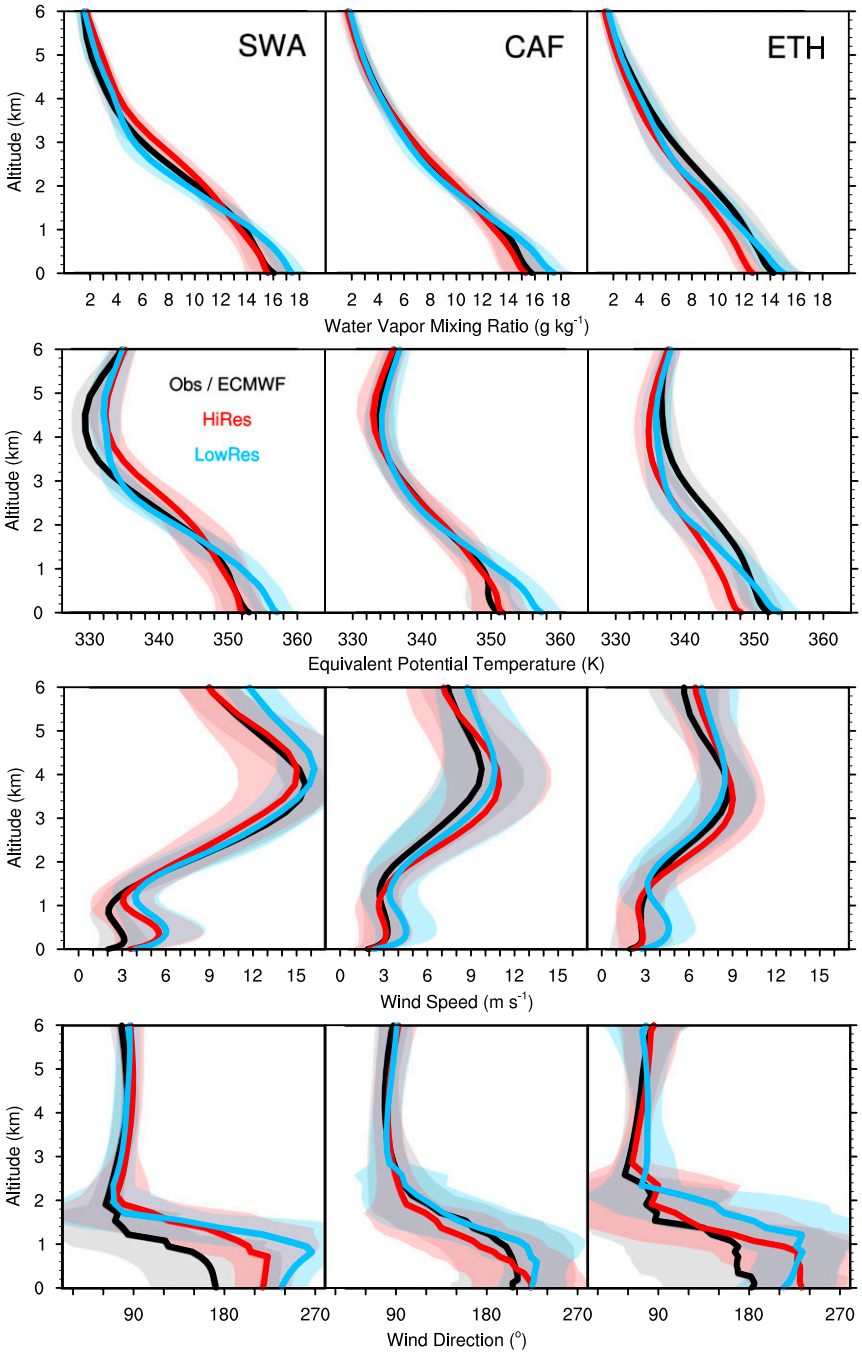

FIG. 11. Mean vertical profiles of (from top to bottom) water vapor mixing ratio, equivalent potential temperature, wind speed, and wind direction for long-lived MCSs for each subregion: (left) SWA, (middle) CAF, and (right) ETH. The subregions are shown in Fig. 4a. The profiles are computed 6 h before the long-lived MCSs detection. The shaded contours show the standard deviation for each dataset.

occur off the Atlantic coast, as has also been obtained with TRMM climatology (Janiga and Thorncroft 2014). The total precipitation and its diurnal cycle are partitioned by type of precipitating system here. The observed MCSs produce 66% of the total precipitation over the whole analysis domain. The rest of the precipitation during the 6-day period comes from CACs, isolated convective cells, or other clouds. The long-lived MCSs

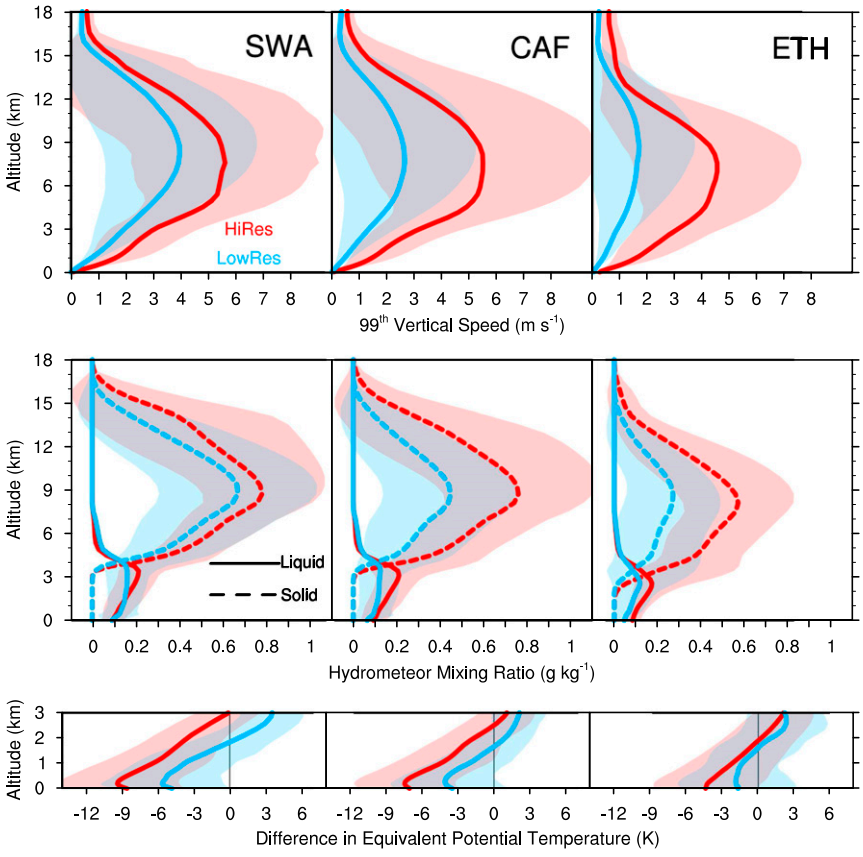

FIG. 12. Mean vertical profiles of (from top to bottom) 99th percentile of the vertical wind speed, mean hydrometeor mixing ratio (liquid and solid) for long-lived MCSs, and difference of mean equivalent temperature inside the long-lived MCSs and at the same location 6 h before, for (left) SWA, (middle) CAF, and (right) ETH. The shaded contours show the standard deviation for each dataset.

produce 55% of total precipitation. They mainly explain the diurnal cycle of continental precipitation, which peaks in the evening. Furthermore, they are the first contributor to nocturnal precipitation, as well-developed MCSs can sustain themselves for several hours when surface fluxes are strongly reduced. Overall, the number of long-lived MCSs decreases with increasing lifetime. The number, effective diameter, and propagative properties of the long-lived MCSs have been further analyzed by subregion. The westward long-lived MCSs present a southward component over SWA. They are the largest, fastest, and longest-lived when compared to CAF and ETH. The AEJ increases in strength from ETH to SWA, in turn increasing the vertical shear, a key mechanism in the organization of convection. SWA also presents the greatest conditional instability. To the authors' knowledge, this is the first time that the partition of total precipitation and its diurnal cycle by type of precipitating system over eastern Africa have been investigated together with the environmental conditions of the long-lived MCSs.

The convection-permitting simulation mimics the zonal distribution of continental precipitation well. It succeeds correctly partitioning precipitation among the different types of precipitating systems, with 50% of the total precipitation due to long-lived MCSs. The long-lived MCSs are also the main contributors to nocturnal precipitation over land. The latter is, however, underestimated. The lack of nighttime continental precipitation results from a systematic deficit in precipitation over SWA and CAF, which is compensated by an excess over ETH during the afternoon and early evening. This precipitation surplus over ETH comes from the afternoon triggering of too many long-lived MCSs. Over SWA, the deficit in precipitation is due to the reduced effective diameter and lifetime of the long-lived MCSs, which are one-third and half of what is observed, respectively. As SWA presents the greatest conditional instability, the

long-lived MCSs are the most vigorous, with greater upward velocities and hydrometeor loading than over CAF or ETH. The strong AEJ and shear, well reproduced over SWA, appear not to be sufficient to sustain long-lived MCSs that are as large, fast and long as observed. We suggest that the reported wet bias around 3-km altitude over SWA would lead to the lack of organization of the long-lived MCSs. This wet bias may be explained by an incorrect location of the long-lived MCSs with respect to the AEWs. This would, in turn, cause the erroneous propagation of the long-lived MCSs, whose propagation direction presents a northward meridional component.

The simulation with parameterized convection fails to reproduce both the partition of precipitation and its diurnal cycle. Clouds other than DCCs are the first contributors to precipitation and the diurnal cycle peaks at 1500 LST, too early in the afternoon. This is due to the deep convection parameterization, which produces 70% of the total precipitation of the simulation, but the cloud content generated by the parameterization is not high enough to simulate the BT correctly (i.e., to simulate BT low enough to be included in the DCC category). A consequence is that the DCC contribution to the total precipitation, and its diurnal cycle, is too low. The remaining 30% of precipitation results from the explicit upward transport of humidity and its microphysical transformations. It shows a fairly negligible diurnal variability but still contributes to the increase in total precipitation during the evening and the night. The too early precipitation peak nevertheless represents an improvement with respect to the diurnal cycle of precipitation in global circulation models (Guichard et al. 2004). The simulation with parameterized convection is able to simulate long-lived MCSs, which are not generally produced by other models with convective parameterization, but they only contribute to one-third of precipitation and are too small, and have too low a zonal speed and too short a lifetime. They also present much lower vertical speeds and hydrometeor contents than in the convection-permitting simulation.

This study shows that the long-lived MCSs are the main contributors to precipitation over northern Africa from 9 to 14 June 2006. The convection-permitting simulation is successful in reproducing the precipitation partition, whereas the simulation with parameterized convection fails. This result highlights the added value gained by representing the convection explicitly. This study also shows that the convection is more organized over West Africa than over eastern Africa. The convection-permitting simulation fails to represent the zonal increase in organization and shows too many tracks of long-lived MCSs, a drawback also seen over West Africa with the convection-permitting Applications of Research to Operations at Mesoscale (AROME) model (Beucher et al. 2014). We suggest that this is the consequence of a wet anomaly around 3-km altitude. It is also possible that the lack of precipitation from the less-organized, long-lived MCSs prevents the drying of the atmosphere there. The excessive number of MCSs in convection-permitting simulations has been identified in other areas [i.e., over Brazil (Machado and Chaboureau 2015) and the southern United Kingdom (Hanley et al. 2015)]. These studies pointed out the sensitivity of MCS organization to the subgrid turbulence scheme. Finally, the conclusions drawn from this study are based on a specific 6-day case over a region that experiences very large seasonal changes as well as significant intraseasonal variability. It would be worthwhile to repeat the assessment made here for other cases or over longer periods in order to disentangle the role of the environment from the effect of some systematic model errors.

Acknowledgments. The research leading to these results has received funding from the European Union Seventh Framework Program (FP7/2007-2013) under Grant 603502 (EU project DACCIWA: Dynamics-aerosol-chemistry-cloud interactions in West Africa). Computer resources were allocated by GENCI through Project 90569. We thank the anonymous reviewers for their comments, which helped to improve the overall quality of the paper.

REFERENCES

Bayo Omotosho, J., 1985: The separate contributions of line squalls, thunderstorms and the monsoon to the total rainfall in Nigeria. *J. Climatol.*, **5**, 543–552, https://doi.org/10.1002/joc.3370050507.

Bechtold, P., E. Bazile, F. Guichard, P. Mascart, and E. Richard, 2001: A mass-flux convection scheme for regional and global models. *Quart. J. Roy. Meteor. Soc.*, **127**, 869–886, https://doi.org/10.1002/qj.49712757309.

Beucher, F., J.-P. Lafore, F. Karbou, and R. Roca, 2014: High-resolution prediction of a major convective period over West Africa. *Quart. J. Roy. Meteor. Soc.*, **140**, 1409–1425, https://doi.org/10.1002/qj.2225.

Chaboureau, J.-P., and P. Bechtold, 2005: Statistical representation of clouds in a regional model and the impact on the diurnal cycle of convection during Tropical Convection, Cirrus and Nitrogen Oxides (TROCCINOX). *J. Geophys. Res.*, **110**, D17103, https://doi.org/10.1029/2004JD005645.

——, P. Tulet, and C. Mari, 2007: Diurnal cycle of dust and cirrus over West Africa as seen from Meteosat Second Generation satellite and a regional forecast model. *Geophys. Res. Lett.*, **34**, L02822, https://doi.org/10.1029/2006GL027771.

——, and Coauthors, 2008: A midlatitude precipitating cloud database validated with satellite observations. *J. Appl. Meteor. Climatol.*, **47**, 1337–1353, https://doi.org/10.1175/2007JAMC1731.1.

——, and Coauthors, 2016: Fennec dust forecast intercomparison over the Sahara in June 2011. *Atmos. Chem. Phys.*, **16**, 6977–6995, https://doi.org/10.5194/acp-16-6977-2016.

Crumeyrolle, S., and Coauthors, 2011: Transport of dust particles from the Bodélé region to the monsoon layer—AMMA case

study of the 9–14 June 2006 period. *Atmos. Chem. Phys.*, **11**, 479–494, https://doi.org/10.5194/acp-11-479-2011.

Cuxart, J., P. Bougeault, and J.-L. Redelsperger, 2000: A turbulence scheme allowing for mesoscale and large-eddy simulations. *Quart. J. Roy. Meteor. Soc.*, **126**, 1–30, https://doi.org/10.1002/qj.49712656202.

Fink, A. H., and A. Reiner, 2003: Spatiotemporal variability of the relation between African Easterly Waves and West African Squall Lines in 1998 and 1999. *J. Geophys. Res.*, **108**, 4332, https://doi.org/10.1029/2002JD002816.

——, D. G. Vincent, and V. Ermert, 2006: Rainfall types in the West African Sudanian Zone during the summer monsoon 2002. *Mon. Wea. Rev.*, **134**, 2143–2164, https://doi.org/10.1175/MWR3182.1.

Flamant, C., C. Lavaysse, M. Todd, J.-P. Chaboureau, and J. Pelon, 2009: Multi-platform observations of a representative springtime case of Bodélé and Sudan dust emission, transport and scavenging over West Africa. *Quart. J. Roy. Meteor. Soc.*, **135**, 413–430, https://doi.org/10.1002/qj.376.

Fouquart, Y., and B. Bonnel, 1986: Computations of solar heating of the Earth's atmosphere: A new parametrization. *Beitr. Phys. Atmos.*, **53**, 35–62.

Futyan, J. M., and A. D. Del Genio, 2007: Deep convective system evolution over Africa and the tropical Atlantic. *J. Climate*, **20**, 5041–5060, https://doi.org/10.1175/JCLI4297.1.

Goyens, C., D. Lauwaet, M. Schröder, M. Demuzere, and N. P. M. Van Lipzig, 2012: Tracking mesoscale convective systems in the Sahel: Relation between cloud parameters and precipitation. *Int. J. Climatol.*, **32**, 1921–1934, https://doi.org/10.1002/joc.2407.

Grini, A., P. Tulet, and L. Gomes, 2006: Dusty weather forecasts using the Méso-NH mesoscale atmospheric model. *J. Geophys. Res.*, **111**, D19205, https://doi.org/10.1029/2005JD007007.

Guichard, F., and Coauthors, 2004: Modelling the diurnal cycle of deep precipitating convection over land with cloud-resolving models and single-column models. *Quart. J. Roy. Meteor. Soc.*, **130**, 3139–3172, https://doi.org/10.1256/qj.03.145.

Hanley, K. E., R. S. Plant, T. H. M. Stein, R. J. Hogan, J. C. Nicol, H. W. Lean, C. Halliwell, and P. A. Clark, 2015: Mixing-length controls on high-resolution simulations of convective storms. *Quart. J. Roy. Meteor. Soc.*, **141**, 272–284, https://doi.org/10.1002/qj.2356.

Huffman, G. J., and Coauthors, 2007: The TRMM Multisatellite Precipitation Analysis (TMPA): Quasi-global, multiyear, combined-sensor precipitation estimates at fine scales. *J. Hydrometeor.*, **8**, 38–55, https://doi.org/10.1175/JHM560.1.

Janiga, M. A., and C. D. Thorncroft, 2014: Convection over tropical Africa and the east Atlantic during the West African Monsoon: Regional and diurnal variability. *J. Climate*, **27**, 4159–4188, https://doi.org/10.1175/JCLI-D-13-00449.1.

Janowiak, J. E., R. J. Joyce, and Y. Yarosh, 2001: A real-time global half-hourly pixel resolution infrared dataset and its applications. *Bull. Amer. Meteor. Soc.*, **82**, 205–217, https://doi.org/10.1175/1520-0477(2001)082<0205:ARTGHH>2.3.CO;2.

Lafore, J. P., and Coauthors, 1998: The Méso-NH Atmospheric Simulation System. Part I: Adiabatic formulation and control simulations. *Ann. Geophys.*, **16**, 90–109, https://doi.org/10.1007/s00585-997-0090-6.

Laing, A. G., R. Carbone, V. Levizzani, and J. Tuttle, 2008: The propagation and diurnal cycles of deep convection in northern tropical Africa. *Quart. J. Roy. Meteor. Soc.*, **134**, 93–109, https://doi.org/10.1002/qj.194.

Lemaître, C., C. Flamant, J. Cuesta, J.-C. Raut, P. Chazette, P. Formenti, and J. Pelon, 2010: Radiative heating rates profiles associated with a springtime case of Bodélé and Sudan dust transport over West Africa. *Atmos. Chem. Phys.*, **10**, 8131–8150, https://doi.org/10.5194/acp-10-8131-2010.

Machado, L. A. T., and J.-P. Chaboureau, 2015: Effect of turbulence parameterization on assessment of cloud organization. *Mon. Wea. Rev.*, **143**, 3246–3262, https://doi.org/10.1175/MWR-D-14-00393.1.

——, W. B. Rossow, R. L. Guedes, and A. W. Walker, 1998: Life cycle variations of mesoscale convective systems over the Americas. *Mon. Wea. Rev.*, **126**, 1630–1654, https://doi.org/10.1175/1520-0493(1998)126<1630:LCVOMC>2.0.CO;2.

Masson, V., and Coauthors, 2013: The SURFEXv7.2 land and ocean surface platform for coupled or offline simulation of earth surface variables and fluxes. *Geosci. Model Dev.*, **6**, 929–960, https://doi.org/10.5194/gmd-6-929-2013.

Mathon, V., H. Laurent, and T. Lebel, 2002: Mesoscale convective system rainfall in the Sahel. *J. Appl. Meteor.*, **41**, 1081–1092, https://doi.org/10.1175/1520-0450(2002)041<1081:MCSRIT>2.0.CO;2.

Mlawer, E. J., S. J. Taubman, P. D. Brown, M. J. Iacono, and S. A. Clough, 1997: Radiative transfer for inhomogeneous atmospheres: RRTM, a validated correlated-k model for the longwave. *J. Geophys. Res.*, **102**, 16 663–16 682, https://doi.org/10.1029/97JD00237.

Pantillon, F., P. Mascart, J.-P. Chaboureau, C. Lac, J. Escobar, and J. Duron, 2011: Seamless MESO-NH modeling over very large grids. *C. R. Mec.*, **339**, 136–140, https://doi.org/10.1016/j.crme.2010.12.002.

Pergaud, J., V. Masson, S. Malardel, and F. Couvreux, 2009: A parameterization of dry thermals and shallow cumuli for mesoscale numerical weather prediction. *Bound.-Layer Meteor.*, **132**, 83–106, https://doi.org/10.1007/s10546-009-9388-0.

Pinty, J.-P., and P. Jabouille, 1998: A mixed-phase cloud parameterization for use in a mesoscale non-hydrostatic model: Simulations of a squall line and of orographic precipitation. *Conf. on Cloud Physics*, Everett, WA, Amer. Meteor. Soc., 217–220.

Saunders, R., M. Matricardi, P. Brunel, S. English, P. Bauer, U. O'Keeffe, P. Francis, and P. Rayer, 2005: RTTOV-8 science and validation report. Tech. Rep., NWP SAF Rep., 41 pp.

Segele, Z. T., and P. J. Lamb, 2005: Characterization and variability of Kiremt rainy season over Ethiopia. *Meteor. Atmos. Phys.*, **89**, 153–180, https://doi.org/10.1007/s00703-005-0127-x.

Skamarock, W. C., 2004: Evaluating mesoscale NWP models using kinetic energy spectra. *Mon. Wea. Rev.*, **132**, 3019–3032, https://doi.org/10.1175/MWR2830.1.

Söhne, N., J.-P. Chaboureau, and F. Guichard, 2008: Verification of cloud cover forecast with satellite observation over West Africa. *Mon. Wea. Rev.*, **136**, 4421–4434, https://doi.org/10.1175/2008MWR2432.1.

Tian, B., B. J. Soden, and X. Wu,2004: Diurnal cycle of convection, clouds, and water vapor in the tropical upper troposphere: Satellites versus a general circulation model. *J. Geophys. Res.*, **109**, D10101, https://doi.org/10.1029/2003JD004117.

Tompkins, A. M., C. Cardinali, J.-J. Morcrette, and M. Rodwell, 2005: Influence of aerosol climatology on forecasts of the African Easterly Jet. *Geophys. Res. Lett.*, **32**, L10801, https://doi.org/10.1029/2004GL022189.

WMO, 2014: WMO guide to meteorological instruments and methods of observation. Part I: Measurement of meteorological variables. Tech. Rep. WMO-8, 1177 pp., https://library.wmo.int/opac/doc_num.php?explnum_id=4147.

Zhang, G., K. H. Cook, and E. K. Vizy, 2016: The diurnal cycle of warm season rainfall over West Africa. Part I: Observational analysis. *J. Climate*, **29**, 8423–8437, https://doi.org/10.1175/JCLI-D-15-0874.1.